Low-Dose CT Image Processing Using Artifact Suppressed Total Generalized Variation

Shangguan Hong[1,2,3], Anhong Wang[1], Xiong Zhang[1], Zhiguo Gui[1,2,3,*]

[1]School of electronic information engineering
Taiyuan University of Science and Technology, Taiyuan 030024, China
shangguan_hong01@163.com

[2]Science and Technology on Electronic Test and Measurement Laboratory
North University of China, Taiyuan 030051, China

[3]Key Laboratory of Instrumentation Science & Dynamic Measurement
North University of China, Taiyuan 030051, China
*Corresponding author: gzgtg@163.com

ABSTRACT. *The improvement of low-dose computed tomography (LDCT) images degraded by amplified mottle noise and streak artifacts without introducing tissue-blurring effects remains a challenge that needs to be overcome. In this paper, we propose to process LDCT images by using an adaptive total generalized variation algorithm based on strict intuitionistic fuzzy entropy. Firstly, considering the fuzziness of an artifact-degraded LDCT image, a membership function based on strict intuitionistic fuzzy entropy was constructed to replace the traditional diffusion coefficient function. Secondly, an adaptive TGV regularized LDCT image restoration model based on the constructed diffusion coefficient function was presented. Next, to solve the two difficulties, namely the solution of the adaptive diffusion coefficient with implicit estimation problem and the joint regularization TGV estimation model with dual variables, in the optimization estimation process of the proposed algorithm model, in this work, a particle swarm optimization (PSO) algorithm and first-order primal-dual algorithm were utilized, respectively. Finally, experiments on LDCT images with three kinds of streak artifact distribution were carried out. The results show that the proposed algorithm can suppress the noise and streak artifact while preserving the important edges of the image.*
Keywords: Low-dose CT, Total generalized variation, Intuitionistic fuzzy entropy, Artifact suppression

1. **Introduction.** In recent years, X-ray computed tomography (CT) imaging technology has made rapid development, and has gradually become an indispensable means of imaging in the field of medical diagnosis and treatment, image guided intervention, industrial non-destructive testing and other fields[1]. CT images are characterized by their high-resolution, high-sensitivity, and multi-slice properties; therefore, they can clearly show the structure and lesions of the brain, spinal cord, pancreas, and other organs[2]. A survey shows that repeated CT scanning is the main source of iatrogenic radiation, and the patient will be exposed to X-rays at doses of approximately 1.5 to 20 mSv (millisievert) on a routine CT examination[3]. The radiation damage caused by CT examination should not be underestimated. Potential hazards associated with X-ray radiation include metabolic abnormalities, cancer, leukemia, and other genetic disorders[4].

Reducing the scanning dose in CT examination has become an urgent task, but dose reduction often causes LDCT images to be seriously degraded by amplified mottle noise and non-stationary streak artifacts[5]. Since most artifacts have position-dependent distributions and amplitudes similar to those of normal attenuating structures, it is rather challenging to suppress artifacts and remove noise in LDCT images. Streak artifacts, which are always characterized by relatively prominent intensity features, can significantly decrease the distinction between normal tissues and lesions[6]. Many post-processing methods have been proposed in an attempt to obtain LDCT images with acceptable noise-removal, artifact-suppression, and edge preservation. Because off-line processing can be directly operated on LDCT images, these kinds of methods may greatly reduce the requirements for real-time imaging and huge storage space[7,8].

Over the past decade, many state-of-the-art denoising approaches have been proposed including total generalized variation (TGV)-based methods[9,10], non-local means-based filters[11], and sparse representation-based methods[12]. For example, Chen et al.[13] proposed a noise reduction method for low-dose CT via a deep neural network without the need to process the original projection data. A deep convolutional neural network is trained to transform low-dose CT images into normal-dose CT images, patch by patch. Cui et al.[14] formulated streak artifacts removal as an image decomposition problem based on morphological component analysis (MCA). Their method contributed to decompose artifacts from the high-frequency parts by using automatic and self-contained dictionary learning, where no additional training samples are required. Ha et al.[15] advocated to take into consideration the vast body of external knowledge that exists in the domain of already acquired medical CT images, and incorporated this knowledge by creating a database of prior scans, either of the same patient or a diverse corpus of different patients, to assist in the image restoration process.

By storing a diverse set of small image patches in conjunction with a localized similarity-matching scheme, their global database approach is sufficiently strong to yield good similarity matches from the database and as a direct effect, produce image restorations of high quality. Zhang et al.[16] proposed an effective algorithm for quantum noise removal in LDCT images using shearlet transform. Shi et al.[17] proposed a low-dose cardiac CT processing method based on three-dimensional sparse representation theory. By utilizing the correlation between anatomical structures, the spatially and temporally continuous information of the image was integrated into a sparse representation. Since the noise and artifact distribution of LDCT images are not regular and there is no strict continuity, this method can suppress the noise and artifacts well while preserving the important details and edges of LDCT images. Chen et al.[5] proposed a post-processing method based on dictionary learning to improve the quality of LDCT images. Based on the analysis of the difference between artifacts and structural details, a so-called discriminative dictionary was obtained, which uses a sparse representation of the dictionary to filter the artifacts in all directions, and then, through the global dictionary learning process, filter residual artifacts and noise. In addition, some attention was paid to improving the training dictionary speed. Chen et al.[18] proposed a rapid post-processing method for LDCT images of abdominal tumors based on patch-based dictionary learning.

The main goal of LDCT image restoration is to suppress the mottle noise and streak artifacts as much as possible while not introducing new noise and artifacts on condition that it preserves the original edges and structures. In general, since the artifacts in LDCT images have position-dependent distributions and have different intensities, structures, and directions, it is difficult to accurately establish a statistical model. Therefore, the ability to effectively distinguish among noise, artifacts, normal anatomical structures, and lesions

will remain the focus of future research in this field. A growing interest in TGV regularization methods[9,10] has recently been observed. Compared to total variation (TV) regularization methods, which allow the existence of discontinuous solutions but tend to have an obvious piecewise constant effect in their steady-state solution, TGV is capable of measuring directional features and image high-order characteristics and measure image characteristics up to a certain degree of differentiation[19,20]. Some successful applications in medical imaging have been explored for TGV-based approaches[21]. Duan et al.[22] proposed a second-order Mumford-Shah total generalized variation (MSTGV) model that combines the original -convergence approximated MS model with TGV regularization. The incorporation of TGV regularization can eliminate both the staircase artifact associated with the first-order TV regularization and the edge blurring effect associated with the H1 or second-order bounded Hessian regularization. Respectively, utilizing TGV and its dual TGV* to model the cartoon and oscillation components, Lu et al.[23] presented a method for separating images into piecewise cartoon and texture parts, exploiting both the variational mechanism and Yves Meyers modeling principle for oscillating patterns.

In this work, an adaptive total generalized variation algorithm based on strict intuitionistic fuzzy entropy was proposed, aiming to introduce the advantages of fuzzy theory and incorporate smoothness up to a certain differential order, while still accounting for edges. Firstly, based on the fuzziness of LDCT images, strict intuitionistic fuzzy entropy was constructed to represent the uncertainty of LDCT images. Secondly, considering the problem that it is difficult to effectively distinguish among artifacts, normal anatomical structures, and the lesions caused by the complexity of LDCT image artifact distribution, the membership function of the gradient norm to the flat region was used as the diffusion coefficient to adaptively judge the edges and flat regions. Furthermore, an adaptive TGV regularization image restoration algorithm based on strict intuitionistic fuzzy entropy was proposed. In addition, to solve the two difficulties, namely the solution of the adaptive diffusion coefficient with implicit estimation problem and the joint regularization TGV estimation model with dual variables, the particle swarm optimization (PSO) algorithm and first-order primal-dual algorithm, respectively, were utilized in this work in the optimization estimation process of the proposed algorithm model. Finally, experiments on LDCT images with three kinds of streak artifact distribution were carried out. The structure of this paper is as follows: In section 2, background concepts related to our method are reviewed. In section 3, we describe the proposed approach and algorithm analysis. In section 4 the experimental results are given and discussed. Conclusions and plans for future work are outlined in section 5.

2. **2. Related work.**

2.1. **TV.** Generally, for an ideal image u, which is defined on a bounded domain and measured in the presence of additive noise n, the measured noisy f is cast in the form

$$f = u + n \qquad (1)$$

It is necessary to address the image denoising problem: Remove the noise from f and obtain results as close as possible to the original image u. The least-squares (LS) approximation: $\inf_u \left\{ \int_\Omega |f(x) - u(x)|^2 dx \right\}$ is a traditional solution to this problem. The method that is usually used to overcome the ill-condition of LS is the regularization method, of which the basic idea is: introducing a regularization into the objective function of the ill-conditioned problem to make the regularization problem be in a good condition, and then using the solution of the regularization problem to approximate the solution of the

ill-conditioned problem[24]. On a Banach space

$$L^p(\Omega) = \left\{ u(x), x \in \Omega : \int_\Omega |\nabla u(x)|^p dx < \infty \right\} (1 \le p < \infty) \tag{2}$$

the norm is defined as $\|u(x)\|_{L^p(\Omega)} = \left(\int_\Omega |u(x)|^p dx \right)^{1/p}$. On this basis, an image can be described as:

$$H^1(\Omega) = \left\{ u(x) \in L^2(\Omega) : \nabla u(x) = \left(\frac{\partial u}{\partial x_1}, \frac{\partial u}{\partial x_2} \right) \in L^2(\Omega) \times L^2(\Omega) \right\} \tag{3}$$

. The mathematical formulation of the denoising problem is cast in the form

$$\inf_{u \in H^1(\Omega)} \left\{ \|f - u\|_{L^2(\Omega)}^2 + \beta \int_\Omega |\nabla u|^2 dx \right\} \tag{4}$$

, where $\|f - u\|_{L^2(\Omega)}^2$ is the data fidelity, which ensures that the recovered image retains the main features of the image to be recovered f. The regularization term $\int_\Omega |\nabla u|^2 dx$ is actually the square of a semi-module on the $H^1(\Omega)$, which is used to remove the noise and to ensure that the minimization problem is in a good condition. Because it requires very high smoothness of images and does not allow discontinuous or singular features such as edges in images, the Sobolev space is only suitable for describing smooth and uniform regions in images. Actually, the inherent characteristic of an image is the presence of a mutation (edge). If the $\int |\nabla u|^2$ was used as the smoothing item, it will particularly emphasize the penalty for areas with larger gradient values, which is incompatible with the inherent characteristics of the image. The bounded variation (BV) function or distribution space uses the gradient of an image as a measure instead of a function, which allows the image to have important discontinuity features such as edges and textures. It is more reasonable to use BV space to describe the global regularity of the image. On a bounded domain $\Omega \subset \mathbb{R}^2$, $u \in L^1(\Omega)$, and then the total variation of u is defined as

$$\int_\Omega |Du| = \sup \left\{ \int_\Omega u \, div\varphi dx : \varphi = (\varphi_1, \varphi_2) \in C_0^1(\Omega) \times C_0^1(\Omega), |\varphi|_{L^\infty(\Omega)} \le 1 \right\} \tag{5}$$

where $div\varphi = \frac{\partial \varphi_1}{\partial x_1} + \frac{\partial \varphi_2}{\partial x_2}$, is the Lebesgue measure on $\mathbb{R}^2$, $C_0^1(\Omega)$ is the first-order continuously differentiable and tightly supported functions defined on . In particular, $\forall u \in C^1(\Omega)$, $\int_\Omega u \, div\varphi dx = -\int_\Omega \nabla u \cdot \varphi dx$, where $\nabla u \cdot \varphi$ represents the Euclidean inner product of two two-dimensional vectors. Further, $\int_\Omega |Du| = \int_\Omega |\nabla u(x)| dx$, $\nabla u = \left(\frac{\partial u}{\partial x_1}, \frac{\partial u}{\partial x_2} \right)$. If the bounded variational function space is defined as:

$$BV(\Omega) = \left\{ u \in L^1(\Omega) : \int_\Omega |Du| dx < \infty \right\} \tag{6}$$

The norm on the Banach space $BV(\Omega)$ is defined as $\|u\|_{BV(\Omega)} = \int_\Omega u dx + \int_\Omega |Du| dx$. Rudin et al.[25] used the spatial semi-norm as the smoothing term and for the first time presented the TV regularization image restoration model

$$u = \arg\inf_{u \in BV(\Omega)} \left\{ \frac{1}{2} \|f - u\|_{L^2(\Omega)}^2 + \beta \int_\Omega |u|_{TV} \right\} \tag{7}$$

. Firstly, compute the Euler-Lagrange equation satisfied by u:

$$(f - u) + \beta div \left(\frac{\nabla u}{|\nabla u|} \right) = 0 \tag{8}$$

. Then

$$
\begin{cases}
\dfrac{\partial u}{\partial t}(t;x) = (f(x) - u(t;x)) + \beta div\left(\dfrac{\nabla u}{|\nabla u|}\right)(t;x),\, (t;x) \in (0,T] \times \Omega \\[2mm]
u(0;x) = f(x), & x \in \Omega \\[2mm]
\dfrac{\partial u}{\partial n}(t;x)\Big|_{\partial\Omega} = 0, & (t;x) \in (0,T] \times \partial\Omega
\end{cases}
\tag{9}
$$

. Note$\Delta_-^x u_{i,j} = u_{i,j} - u_{i-1,j}, \Delta_+^x u_{i,j} = u_{i+1,j} - u_{i,j}, \Delta_-^y u_{i,j} = u_{i,j} - u_{i,j-1}, \Delta_+^y u_{i,j} = u_{i,j+1} - u_{i,j}$, the problem Eq.(9) can be solved by the finite difference method

$$div\left(\nabla u_{i,j}^{n+1}/\left|\nabla u_{i,j}^{n+1}\right|\right) \approx div\left(\nabla u_{i,j}^{n+1}/\left|\nabla u_{i,j}^{n}\right|\right)$$

$$
= \frac{1}{h^2}\left(\Delta_-^x\left(\frac{\Delta_+^x u_{i,j}^{n+1}}{\sqrt{\frac{\left(\Delta_+^x u_{i,j}^n\right)^2}{h^2} + \frac{\left(u_{i,j+1}^n - u_{i,j-1}^n\right)^2}{(2h)^2}}}\right) + \Delta_-^y\left(\frac{\Delta_+^y u_{i,j}^{n+1}}{\sqrt{\frac{\left(u_{i+1,j}^n - u_{i-1,j}^n\right)^2}{(2h)^2} + \frac{\left(\Delta_+^y u_{i,j}^n\right)^2}{h^2}}}\right)\right)
\tag{10}
$$

Note

$$
\begin{cases}
c_{i,j}^1 = \beta\Delta t/\sqrt{\left(\left(u_{i+1,j}^n - u_{i,j}^n\right)^2 + \left(u_{i,j+1}^n - u_{i,j-1}^n\right)^2\right)/4}\ , \\[3mm]
c_{i,j}^2 = \beta\Delta t/\sqrt{\left(\left(u_{i,j}^n - u_{i-1,j}^n\right)^2 + \left(u_{i-1,j+1}^n - u_{i-1,j-1}^n\right)^2\right)/4}\ , \\[3mm]
c_{i,j}^3 = \beta\Delta t/\sqrt{\left(u_{i+1,j}^n - u_{i-1,j}^n\right)^2/4 + \left(u_{i,j+1}^n - u_{i,j}^n\right)^2}\ , \\[3mm]
c_{i,j}^4 = \beta\Delta t/\sqrt{\left(u_{i+1,j-1}^n - u_{i-1,j-1}^n\right)^2/4 + \left(u_{i,j}^n - u_{i,j-1}^n\right)^2}
\end{cases}
\tag{11}
$$

Eq.(9) can be discretized as

$$
\begin{aligned}
&- c_{i,j}^1 u_{i+1,j}^{n+1} - c_{i,j}^2 u_{i-1,j}^{n+1} - c_{i,j}^3 u_{i,j+1}^{n+1} - c_{i,j}^4 u_{i,j-1}^{n+1} + \left(1 + c_{i,j}^1 + c_{i,j}^2 + c_{i,j}^3 + c_{i,j}^4\right) u_{i,j}^{n+1} \\
&= u_{i,j}^n + \Delta t\left(f_{i,j} - u_{i,j}^n\right)
\end{aligned}
\tag{12}
$$

Eq.(12) is a semi-implicit difference equation with good stability and can be solved by Gauss-Seidel iteration.

2.2. **TGV.** In 2010, on the basis of the generalized definition of TV Eq. (5), Bredies et al.[20] firstly proposed the definition of the generalized variational TGV:

$$
TGV_\alpha^k(u) = \sup\left\{\int_\Omega u\,div^k\varphi\,dx : \varphi \in C_c^k\left(\Omega, Sym^k\left(\mathbb{R}^d\right)\right), \left\|div^l\varphi\right\|_\infty \le \alpha_l\right\}
\tag{13}
$$

, Where$Sym^k\left(\mathbb{R}^d\right) = \left\{\xi : \underbrace{\mathbb{R}^d \times \cdots \times \mathbb{R}^d}_{k} \to \mathbb{R}\right\}$ represents the symmetric order tensor space.$\alpha = (\alpha_0, \alpha_1, ..., \alpha_{k-1})$ denotes a positive weight, $k \in \mathbb{N}$ is the order of TGV,$l = 0, 1, ..., k-1$.

$$
\left(div^l\varphi\right)_\eta = \sum_{\gamma \in M_l} \frac{l!}{\gamma!}\frac{\partial^l\varphi_{\eta+\gamma}}{\partial x^\gamma}, \forall \eta \in M_{k-1}
\tag{14}
$$

, where$M_k = \left\{\eta \in \mathbb{N}^d\big|\sum_{i=1}^d \eta_i = k\right\}$.$\|\varphi\|_\infty = \sup\left\{\left(\sum_{\eta \in M_k}\frac{k!}{\eta!}\varphi_\eta(x)^2\right)^{\frac{1}{2}}\right\}$ represents the - norm in the symmetric k-order tensor space. When$k = 1, TGV_\alpha^k = \alpha_0 TV$. The k-order
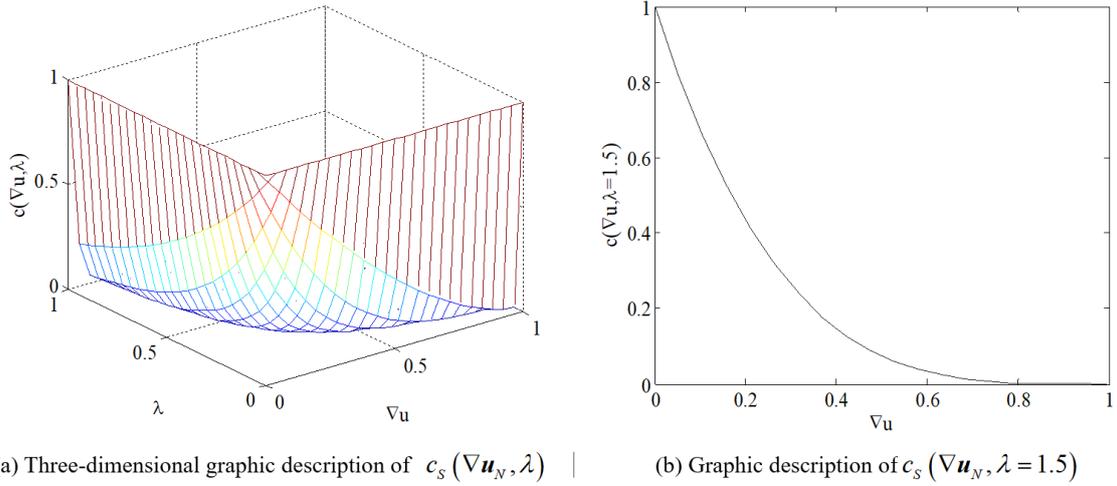
(a) Three-dimensional graphic description of $c_S\left(\nabla \boldsymbol{u}_N, \lambda\right)$ | (b) Graphic description of $c_S\left(\nabla \boldsymbol{u}_N, \lambda = 1.5\right)$

FIGURE 1. Graphic description of the presented adaptive fuzzy diffusion coefficient function $c_S\left(\nabla u_N, \lambda\right)$

bounded generalized variational norm function space $BGV_\alpha^k\left(\Omega\right)$ with weight$\alpha$is defined as:

$$\begin{cases} BGV_\alpha^k\left(\Omega\right) = \left\{ u \in L^1\left(\Omega\right) \middle| TGV_\alpha^k\left(u\right) < \infty \right\} \\ \|u\|_{BGV_\alpha^k(\Omega)} = \|u\|_1 + TGV_\alpha^k\left(u\right) \end{cases} \quad (15)$$

Furthermore, the second-order TGV can be defined as follows:

$$TGV_\alpha^2\left(u\right) = \sup\left\{ \int_\Omega u\, div^2\varphi\, dx : \varphi \in C_c^2\left(\Omega, S^{d\times d}\right), \|\varphi\|_\infty \leq \alpha_0, \|div\varphi\|_\infty \leq \alpha_1 \right\} \quad (16)$$

, where$(div\varphi)_a = \sum_{b=1}^d \frac{\partial \varphi_{ab}}{\partial x_b}, 1 \leq a \leq d$,$div^2\varphi = \sum_{a,b=1}^d \frac{\partial^2 \varphi_{ab}}{\partial x_a \partial x_b}$, and then the inf-norm of$\varphi$and$div\varphi$can be obtained

$$\|\varphi\|_\infty = \sup_{l\in\Omega}\left(\sum_{a,b=1}^d |\varphi_{ab}\left(l\right)|^2\right)^{\frac{1}{2}}, \|div\varphi\|_\infty = \sup_{l\in\Omega}\left(\sum_{b=1}^d |(div\varphi)_b\left(l\right)|^2\right)^{\frac{1}{2}} \quad (17)$$

Then,

$$TGV_\alpha^2\left(u\right) = \inf_{u\in BGV_\alpha^2(\Omega)}\left\{ \sum_{l=1}^2 \alpha_{2-l}\|\varepsilon\left(u_{l-1}\right) - u_l\|_1 \right\} \quad (18)$$

, where$\varepsilon\left(u_{l-1}\right) = \frac{\nabla u_{l-1} + (\nabla u_{l-1})^T}{2}$is a dual variable.$TGV_\alpha^2\left(u\right)$regularized image restoration problems[19,21,26] can be expressed as:

$$\begin{aligned} u &= \min_{u\in BGV_\alpha^2(\Omega)} \frac{1}{2\beta} \int_\Omega \left(u - f\right)^2 dx + TGV_\alpha^2\left(u\right) \\ &= \min_{u\in BGV_\alpha^2(\Omega)} \frac{1}{2\beta} \int_\Omega \left(u - f\right)^2 dx + \alpha_1 \int_\Omega |\nabla u - \varphi| dx + \alpha_0 \int_\Omega |\varepsilon\left(\varphi\right)| dx \end{aligned} \quad (19)$$

Contrary to TV, which can only effectively approach the piecewise constant function, the TGV regularization model can effectively approximate polynomial functions of any order, including slice constants, and slice affine functions.
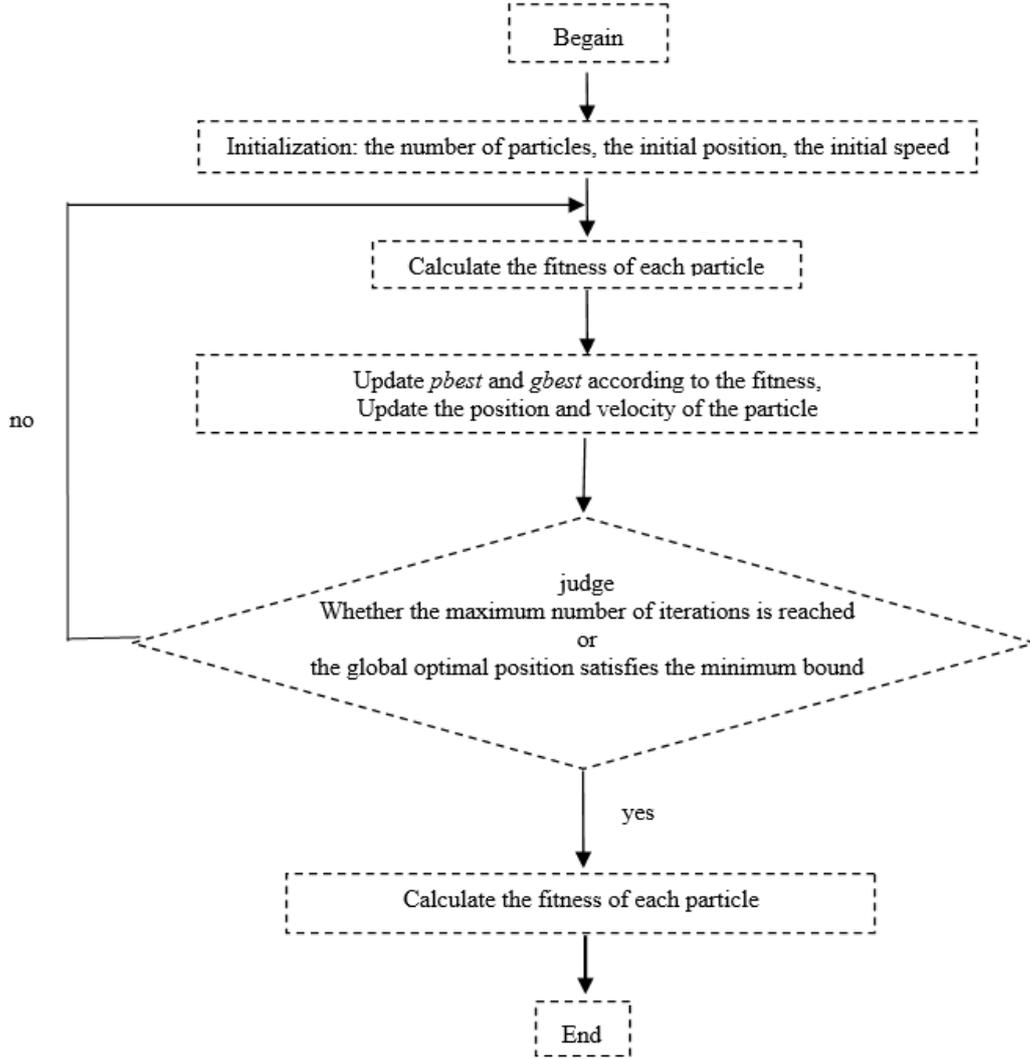
FIGURE 2. Flow chart of PSO algorithm

2.3. **Intuitionistic fuzzy entropy.** According to the intuitionistic fuzzy set theory, an intuitionistic fuzzy set (IFS) A defined on a universe X may be described as

$$A = \{\langle x, \mu_A(x), \gamma_A(x)\rangle | \, x \in X\} \tag{20}$$

, where $\mu_A(x)$ and $\gamma_A(x)$ denote the degree of membership and the degree of non-membership of x to A, respectively. $\mu_A(x)$ denotes the degree of membership of x to A. The degree of uncertainty of x to A can be characterized by an intuitionistic index $\pi_A(x) = 1 - \mu_A(x) - \gamma_A(x)$. If $\pi_A(x)$ is large, it indicates that the element x is very uncertain, and that we know very little about this element. Conversely, if $\pi_A(x)$ is small, it indicates that the element x is very certain, and we know very much about this element. The intuitionistic fuzzy entropy (IFE) is an information quantity which could be used to describe the fuzziness of an IFS. It can be seen that the IFE has the same physical meaning as $\pi_A(x)$. Therefore, when the values of $\mu_A(x)$ and $\gamma_A(x)$ more closely approximate each other, the value of IFE becomes larger. When $\mu_A(x) = \gamma_A(x)$, the IFE could obtain the maximum value 1. Particularly, when $1 - \mu_A(x) = 0$, namely, the intuitionistic index $\pi_A(x) = 0$, and the IFE is 0, the IFE degenerates into a non-fuzzy set at this time[27]. According

to the physical meaning of IFE, scholars have conducted much in-depth study and proposed a variety of IFE construction methods[28-33]. It is shown that there is an inherent deficiency in the definition of IFE, that is, the IFE cannot be used to judge and decide the case that the membership degree and non-membership function are equal but the intuitionistic index is different[34-35]. A strict IFE construction method was proposed to overcome this problem[36-37]. On universe $X = \{x_1, x_2, ..., x_n\}$

$$\begin{cases} IFS(X) = \{\langle x, \mu_A(x), \gamma_A(x)\rangle | \, x \in X\} \\ \mu_A(x) : X \to [0,1] \\ \gamma_A(x) : X \to [0,1] \\ 0 \le \mu_A(x) + \gamma_A(x) \le 1, \forall x \in X \\ \pi_A(x) = 1 - \mu_A(x) - \gamma_A(x) \end{cases} \tag{21}$$

given an intuitionistic fuzzy set $A = \sum\limits_i \langle \mu(x_i), \gamma(x_i)\rangle /x_i$ the strict IFE of A can be expressed by

$$E(A) = \frac{1}{n} \sum_i (\delta(x_i) - \sigma\delta(x_i))(1 - 2\min(\mu(x_i), \gamma(x_i))) \tag{22}$$

(22) where $\delta(x_i) = \frac{1 - |\mu(x_i) - \gamma(x_i)|}{1 + |\mu(x_i) - \gamma(x_i)|}$.

3. Methodology.

3.1. **The constructed fuzzy diffusion coefficient function.** In general, the flat regions and the edges need to be distinctively processed during the image restoration. More concretely, in a flat region, the intensity of the smooth penalty should be sufficiently large to suppress noise and artifacts; however, high-intensity smoothing causes the structure of edges and details to be destroyed in the edges[38]. Thus, the performance of the diffusion coefficient function (or edge indicator function) is particularly important. Low-dose X-ray CT images are uncertain to some extent due to noise and streak artifacts, in other words, the images are fuzzy. Behavioral analysis can be used to demonstrate the similarity between the membership function and the diffusion coefficient in the anisotropic diffusion process[39-42]. Physically speaking, in the smoothing process, if the membership degree of the pixel to the flat region is very large, the pixel is likely to be in the flat region, in which case, a larger diffusion coefficient is needed to promote the smoothing process. Correspondingly, if the membership degree of the pixel to the flat region is very small, the pixel is likely to be in the edges. In order to preserve the edge of the image, a small diffusion coefficient function is needed to prevent the smoothing process. Obviously, the membership function of the pixel to the flat area of the image is consistent with the behavior of the diffusion coefficient function and can be interchanged. In this work, by constructing the strict intuitionistic fuzzy entropy of low-dose CT images, an adaptive fuzzy diffusion coefficient function is presented. Using ∇u represents the gradient of an $I \times J$ image u, the low-dose X-ray CT image can be considered as the following intuitionistic fuzzy set.
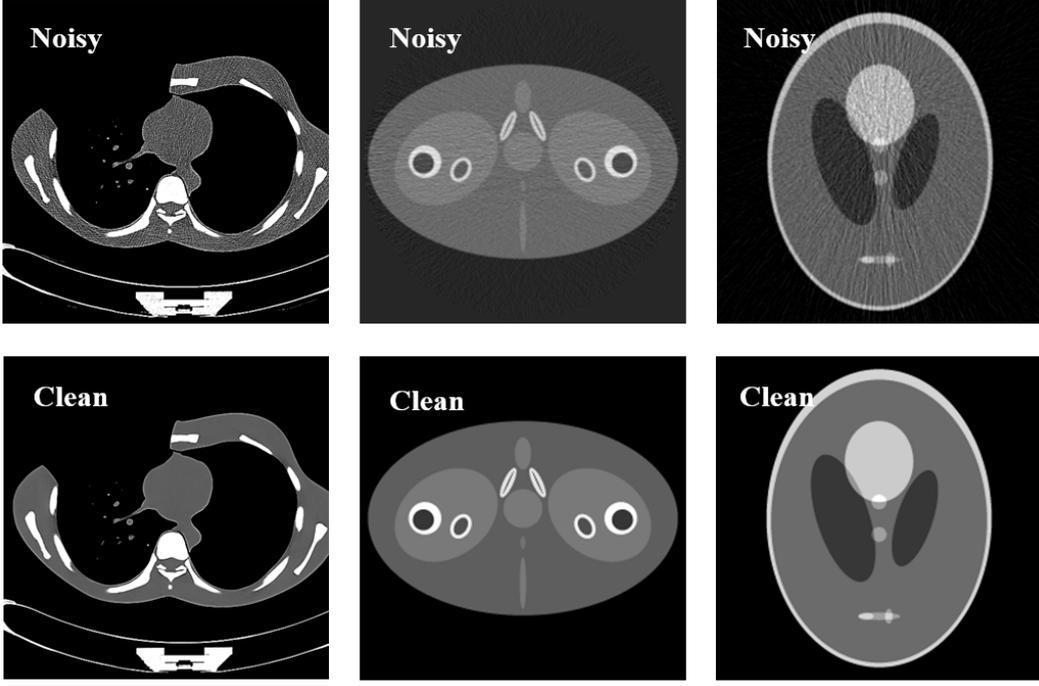
FIGURE 3. Low-dose and standard-dose images of the thoracic CT, the modified Shepp-Logan head model, and the emulational pelvic CT model, respectively

$$\begin{cases} S = \{\langle \nabla u_N, \mu_S\left(\nabla u_N\right), \gamma_S\left(\nabla u_N\right)\rangle | \ \nabla u_S \in U\} \\ \mu_S\left(\nabla u_N\right) = \left(1 - \nabla u_N\right)^{\lambda(\lambda+1)} \\ \gamma_S\left(\nabla u_N\right) = 1 - \left(1 - \nabla u_N\right)^{\lambda} \\ \pi_S\left(\nabla u_N\right) = 1 - \mu_S\left(\nabla u_N\right) - \gamma_S\left(\nabla u_N\right) \\ \nabla u_N = \dfrac{\nabla u - \nabla u_{\min}}{\nabla u_{\max} - \nabla u_{\min}} \end{cases} \tag{23}$$

, where $\mu_S\left(\nabla u_N\right)$ represents the membership function of a pixel to a flat region. $\gamma_S\left(\nabla u_N\right)$ represents the non-membership function of a pixel to a flat region. Assume $x = \nabla u_N$, the following intuitionistic fuzzy entropy can be obtained[43]

$$E_{IF}\left(S\right) = \frac{1}{I \times J} \sum_{i=1}^{I \times J} \frac{2\mu_S\left(x_i\right)\gamma_S\left(x_i\right) + \pi_S(x_i)^2}{\mu_S(x_i)^2 + \gamma_S(x_i)^2 + \pi_S(x_i)^2} \tag{24}$$

. Then, referring to section 3.2, new strict intuitionistic fuzzy entropy was constructed

$$E_{SIF}\left(S, \lambda\right) = \frac{\sum\limits_{i=1}^{I \times J}\left(1 - \sigma\right)\left(\frac{2\mu_S(x_i)\gamma_S(x_i) + \pi_S(x_i)^2}{\mu_S(x_i)^2 + \gamma_S(x_i)^2 + \pi_S(x_i)^2}\right)\left(1 - 2\min\left(\mu_S\left(x_i\right), \gamma_S\left(x_i\right)\right)\right)}{I \times J} \tag{25}$$

. Furthermore, a new adaptive fuzzy diffusion function was presented

$$\begin{cases} c_S\left(\nabla u_N, \lambda\right) = \left(1 - \nabla u_N\right)^{\lambda(\lambda+1)} \\ \lambda = \arg\max\limits_{\lambda} E_{SIF}\left(S, \lambda\right) \end{cases} \tag{26}$$

. Fig.1 shows the graphic description of the presented adaptive fuzzy diffusion coefficient function $c_S(\nabla u_N, \lambda)$. Intuitively, it can be seen that as ∇u_N increases, $c_S(\nabla u_N, \lambda)$ decreases. Thus, $c_S(\nabla u_N, \lambda)$ can enhance the edges and details while suppressing the noise and artifacts in the low-dose CT image.

3.2. **Proposed method and optimization of the objective function.** In order to effectively suppress the noise and artifacts in low-dose X-ray CT images, a novel image processing method using an artifact suppressed total generalized variation is proposed.

$$\hat{u} = \min_{u \in BGV_\alpha^2(\Omega)} \frac{1}{2\beta} \int_\Omega (u - f)^2 dx + \alpha_1 \int_\Omega c_S(\nabla u_N, \lambda) |\nabla u - \varphi| dx + \alpha_0 \int_\Omega |\varepsilon(\varphi)| dx \quad (27)$$

It can be seen that Eq. (27) shows a joint estimation problem. Firstly, to obtain the solution of $c_S(\nabla u_N, \lambda)$, the particle swarm optimization (PSO) method[44-45], which has few parameters, is easy to operate, converges quickly, and seeks the optimal solution by mutual cooperation and information sharing among the individuals in the group, was utilized to solve Eq. (26).

Specifically, as shown in Fig. 2, the algorithm simulates the solving process as a group of birds searching for food. Each optimization solution (particle) is treated as a bird. During the course of the search, the birds continue to change their speed and position (each bird can be judged by the fitness function to determine whether the current speed and position is reasonable), continue to repeat the process, the birds will gradually converge to the best speed to the most optimal position, and then find the food (namely, find the solution of the function). The fitness function of this work is $\lambda = \arg \max_\lambda E_{SIF}(S, \lambda)$. The respective velocity and position of the particles during the iteration are expressed by

$$\begin{cases} V_t = \omega \times V_t + c_1 \times rand \times (pbest_t - \lambda present_t) + c_2 \times rand \times (gbest_t - \lambda present_t) \\ \lambda present_t = \lambda present_t + V_t \end{cases} \quad (28)$$

where the number of particle swarms is T. The velocity and the position of the tth particle are Vt and presentt, respectively and *pbest* and *gbest* are the individual extremum and global extremum, respectively. The $c_S(\nabla u_N, \lambda)$ value can be easily obtained after obtaining the solution of $\lambda = \arg \max_\lambda E_{SIF}(S, \lambda)$. Furthermore, the problem in Eq. (27) can be solved by the first-order primal-dual algorithm[20],

$$\hat{u}^{k+1} = \min_{newu,\omega} \max_{p,q} \frac{1}{2\beta} \|u^n - f\|_2^2 + \langle u^n - \omega, p \rangle - F_1^*(p) + \langle \varepsilon(\omega), q \rangle - F_2^*(q) \quad (29)$$

where

$$\begin{cases} F_1(\nabla u - \omega) = \max_p \langle \nabla u - \omega, p \rangle - F_1^*(p) \\ F_2(\varepsilon(\omega)) = \max_q \langle \varepsilon(\omega), q \rangle - F_2^*(q) \\ \varepsilon(\omega) = 1/2 \left(\nabla \omega + \nabla \omega^T \right) \end{cases}, \quad \begin{cases} P = \left\{ p = (p_1, p_2)^T \middle| |p(x)| \leq \alpha_1 c_S(\nabla u_N, \lambda) \right\} \\ Q = \left\{ q = \begin{pmatrix} q_{11}, q_{12} \\ q_{21}, q_{22} \end{pmatrix}^T \middle| \|q\|_\infty \leq \alpha_0 \right\} \end{cases}$$

The iterative process can then be as follows

$$
\begin{cases}
p^{k+1} = proj_P \left(p^k + \delta \left(\nabla \bar{u}^k - \bar{\omega}^k \right) \right), \\
q^{k+1} = proj_P \left(q^k + \delta \left(\varepsilon \left(\bar{\omega}^k \right) \right) \right), \\
u^{k+1} = prox_1 \left(u^k + \tau div_1 p^{k+1} \right), \\
\omega^{k+1} = \omega^k + \tau \left(p^k + div^\hbar \left(q^{k+1} \right) \right), \\
\bar{u}^{k+1} = u^{k+1} - u^k, \\
\bar{\omega}^{k+1} = 2\omega^{k+1} - \omega^k
\end{cases}
\tag{30}
$$

$$
\begin{cases}
proj_P \left(\hat{p} \right) = \hat{p}/\max \left(1, |\hat{p}|/\alpha_1 c_S \left(\nabla u_N, \lambda \right) \right) \\
proj_Q \left(\hat{q} \right) = \hat{q}/\max \left(1, \hat{q}/\alpha_0 \right) \\
prox_1 \left(u^k \right) = \left(\beta u^k + \tau f^k \right)/(\beta + \tau)
\end{cases}
\tag{31}
$$

where $div^\hbar = -\varepsilon^*$. In summary, the process flow of this work is as follows

Task: Low-dose CT image processing using an artifact suppressed total generalized variation

Parameters: noisy f, β, $\alpha_1, \alpha_0, \delta, \tau, T$ iterations NUM1, NUM2;

Solving process:

(1)   while $n \leq$ NUM1

          Calculate λ by Eq. (28) and the flow chart Fig. 2.

      end

(2)   Calculate $c_S \left(\nabla u_N, \lambda \right)$ by Eq. (26);

(3)   while $k <$ NUM2

          Calculate u^{k+1} by Eq. (31);

          $k = k + 1$;

      end

Output: the quality improved image u.

4. **Results and Discussion.** The feasibility and superiority of the proposed method were verified by conducting experiments using a low-dose X-ray thoracic CT image (512mm ×512mm), a modified Shepp-Logan head model (256mm×256mm) and a low-dose X-ray pelvic CT model (256mm ×256mm). The experimental environment consisted of the following: hardware requirements: CPU: Intel(R) Core(TM) i5, 3.3 GHz; graphics card: Nvidia GeForce GTX 960 (4 GB); RAM: 8 GB; and operating system: Windows 7 64-Bit SP1. The software used was MATLAB 7.6 (R2008a) programming to implement the algorithm. The comparison algorithms adopted by this study are the traditional Perona and Malik (P-M) equation[46] smoothing method (herein referred to TGV), TV regularized image restoration algorithm[25] (herein denoted as TV), TGV regularized image restoration algorithm[26] (herein denoted as TGV). The analysis of experimental results in this work includes three aspects: (1) visual effect analysis; (2) analysis of the quantitative indicators; (3) influence of parameter changes on the experimental results.

4.1. **Thoracic CT experiments.** Apparently, the artifacts in the low-dose CT images shown in Fig. 3 are complex, irregularly distributed, and of varying intensity. As shown in Fig. 4, different algorithms are utilized to process the thoracic CT, resulting in restoration images of varying quality. It can be seen that the PM anisotropic diffusion operation has some effect on the smoothing of noise and artifacts, but the experimental results are far
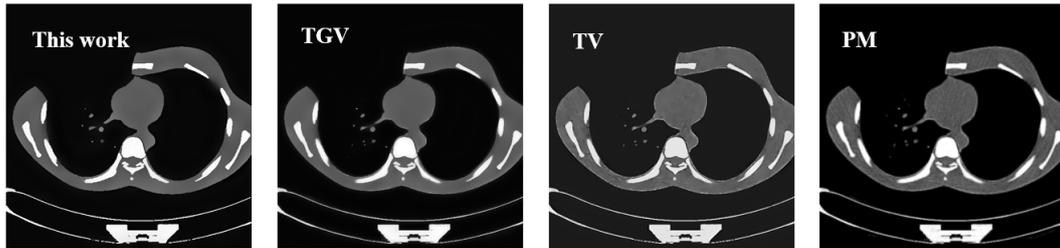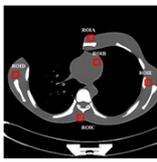
FIGURE 4. Thoracic CT restoration images obtained by four post-processing methods: PM, TV, TGV, and this work, respectively

TABLE 1. rRMSE and SSIM values for the four restoration images in five different ROIs shown in Fig. 4

	ROIA		ROIB		ROIC		ROID		ROIE	
	rRMSE	SSIM	rRMSE	SSIM	rRMSE	SSIM	rRMSE	SSIM	rRMSE	SSIM
This work	0.0077	0.8520	0.0008	0.9741	0.0078	0.7808	0.0019	0.9423	0.0033	0.9446
TGV	0.0078	0.8487	0.0010	0.9735	0.0085	0.7585	0.0024	0.9413	0.0033	0.9321
TV	0.0086	0.8029	0.0028	0.9238	0.0093	0.7534	0.0024	0.8598	0.0047	0.8585
PM	0.0097	0.7388	0.0032	0.8550	0.0097	0.6028	0.0046	0.7148	0.0058	0.7781

from satisfactory. Compared with the PM algorithm, the TV regularization method is more effective in suppressing noise and artifacts. It can be seen intuitively that the TGV regularization method and the algorithm proposed in this work can suppress the noise and strip artifacts very well. The experimental results of the two algorithms are close to the standard dose image quality, which would meet the basic application requirements. Further in-depth analysis of the image consisting of the enlarged local structure of the different thoracic restoration images is shown in Fig. 4, where it can be seen that there are obvious noise and artifacts remaining in the experimental results of the PM algorithm and that smoothing of the diffusion can be expected to cause obvious blurring of the image. Although the TV regularization method suppresses a large number of artifacts and noise, and overcomes the fuzziness of the PM method, there are obvious block artifacts in the local regions of the thoracic CT image. From the point of view of suppression of noise and artifacts, complex bar artifacts and noise in the original degraded image are largely removed in the thoracic restoration images obtained by the TGV regularization method and the method proposed in this work, and no new noise is introduced. Compared with the other three algorithms, the algorithm proposed in this work is mainly superior in terms of the edge preserving aspect. As shown by the white arrow in the observation area, we can see that in the different local regions of the thoracic image, the experimental results have good edge performance.

On the other hand, in order to ensure the objectivity of the experimental analysis, in this research the index relative mean square error (rRMSE) is chosen. This index can represent the degree of closeness between the restoration image and the standard dose image, and structural similarity (SSIM), which can represent the degree of structural
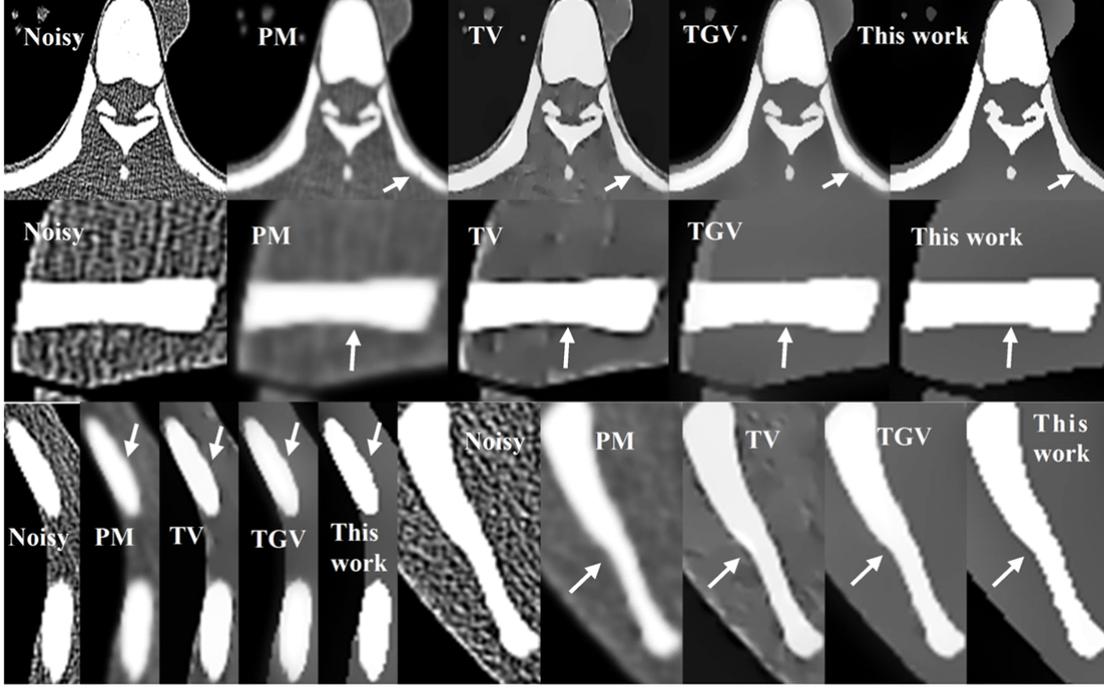
FIGURE 5. Partial enlarged view of the different thoracic CT restoration images (shown in Fig.4)

similarity between the restoration image and standard dose image.

$$rRMSE = \sqrt{\frac{\sum\limits_{m=1}^{M} \left(f_m - f_{xtrue\_m}\right)^2}{\sum\limits_{m=1}^{M} \left(f_{xtrue\_m}\right)^2}} \tag{32}$$

$$Cov\left\{f, f_{xtrue}\right\} = \frac{1}{M-1}\left(f_m - \bar{f}\right)\left(f_{xtrue\_m} - \bar{f}_{xtrue}\right) \tag{33}$$

$$SSIM = \frac{2Cov\left\{f, f_{xtrue}\right\}}{\sigma^2 + \sigma_{xtrue}^2}\frac{2\bar{f}_{xtrue}\bar{f}}{\bar{f}_{xtrue}^2 + \bar{f}^2} \tag{34}$$

where f_m and f_{xtrue_m} represent the restoration image and the standard dose image at pixel m, respectively. M is the total number of pixels of the desired image. A small rRMSE indicates a small difference value between the two comparison images, and vice versa. An SSIM value closer to 1 indicates high structural similarity to the ideal image.

As shown in Table.1, in this research the rRMSE and SSIM values for the four restoration images in five different regions of interest (ROIs) are calculated. Firstly, analyzing the performance of the four kinds of restoration images in each ROI, we can see that the rRMSE value of the restoration image obtained by the method proposed in this work is 0.0077, and are smaller than those of other algorithms: 0.0097, 0.0086, 0.0078, respectively. It indicates that the ROIA of the experimental results obtained by the proposed method is closer to the ROIA of the standard dose image. The SSIM value of the restoration image obtained by the method proposed in this work is 0.8520, and is larger than that of the other algorithms: 0.8487, 0.8029, and 0.7388, respectively. It indicates that the structure of the ROIA of the experimental results obtained by the proposed method is more similar to the structure of the ROIA of the standard dose image. Similarly, the

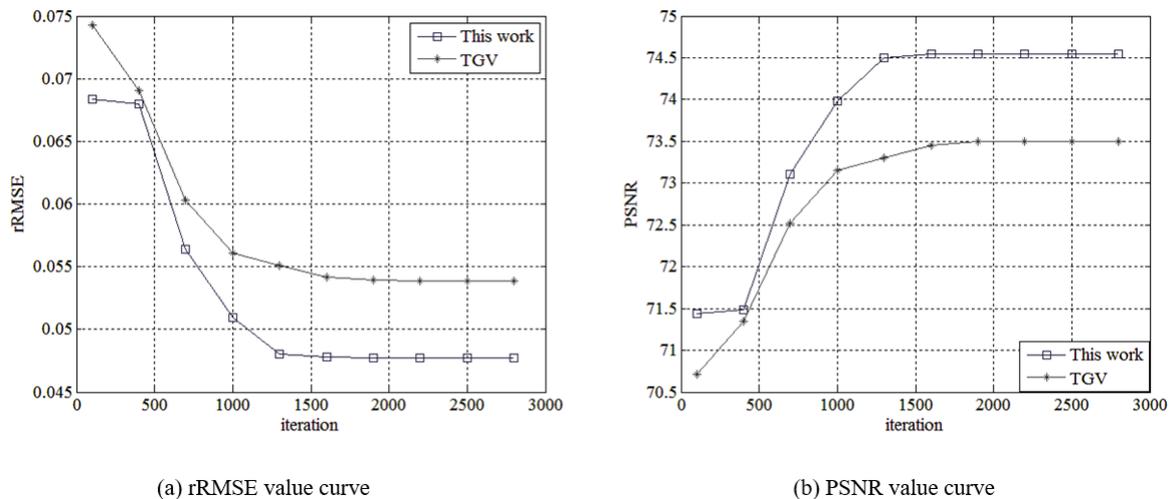(a) rRMSE value curve   (b) PSNR value curve

FIGURE 6. rRMSE and PSNR value curves of results obtained by TGV and the proposed method as a function of the number of iterative cycles NUM2

TABLE 2. PSNR, rRMSE, and SSIM values of the three different ROIs of the four kinds of restoration images (shown in Fig.10)

	ROI1			ROI2			ROI3		
	PSNR	rRMSE	SSIM	PSNR	rRMSE	SSIM	PSNR	rRMSE	SSIM
This work	27.7454	0.0011	0.9994	26.4951	0.0013	0.9960	27.6476	0.0019	0.9907
TGV	27.5632	0.0011	0.9753	25.4231	0.0014	0.8985	27.4392	0.0019	0.9685
TV	26.3874	0.0013	0.7711	23.8668	0.0017	0.8563	26.5400	0.0021	0.8465
PM	24.9256	0.0015	0.4897	24.9232	0.0015	0.6457	26.2546	0.0022	0.6040

rRMSE and SSIM values of the restoration image obtained by the proposed method are the minimum and the maximum of the five ROIs, respectively. It shows that, compared with the experimental results obtained with the other three algorithms, the image quality, structural similarity, and the experimental results of the proposed algorithm are closer to those of the standard dose ideal images. Secondly, analyzing the performance of the each kind of restoration image in different ROIs, we can see that the performance of rRMSE and SSIM in different regions of each kind of restoration image is different. For example, the rRMSE and SSIM values of ROID of the experimental results obtained by the proposed method are 0.0019 and 0.9423, respectively. However, these two values are only 0.0077 and 0.8520 in the ROIA. Obviously, the image quality of ROID is significantly higher than that of ROIA

As a whole, it can be seen that the performance of rRMSE and SSIM may be the same for different restoration images. For example, in ROIE, the rRMSE value of the experimental results obtained by TGV and the proposed method are both 0.0033. In ROID, the rRMSE value of the experimental results obtained by TGV and TV are both 0.0024. Under the same conditions, the experimental results obtained by the proposed method are more accurate. For example, when the rRMSE values are both 0.0033, the SSIM value of the results obtained by the proposed method is 0.9446, which is larger
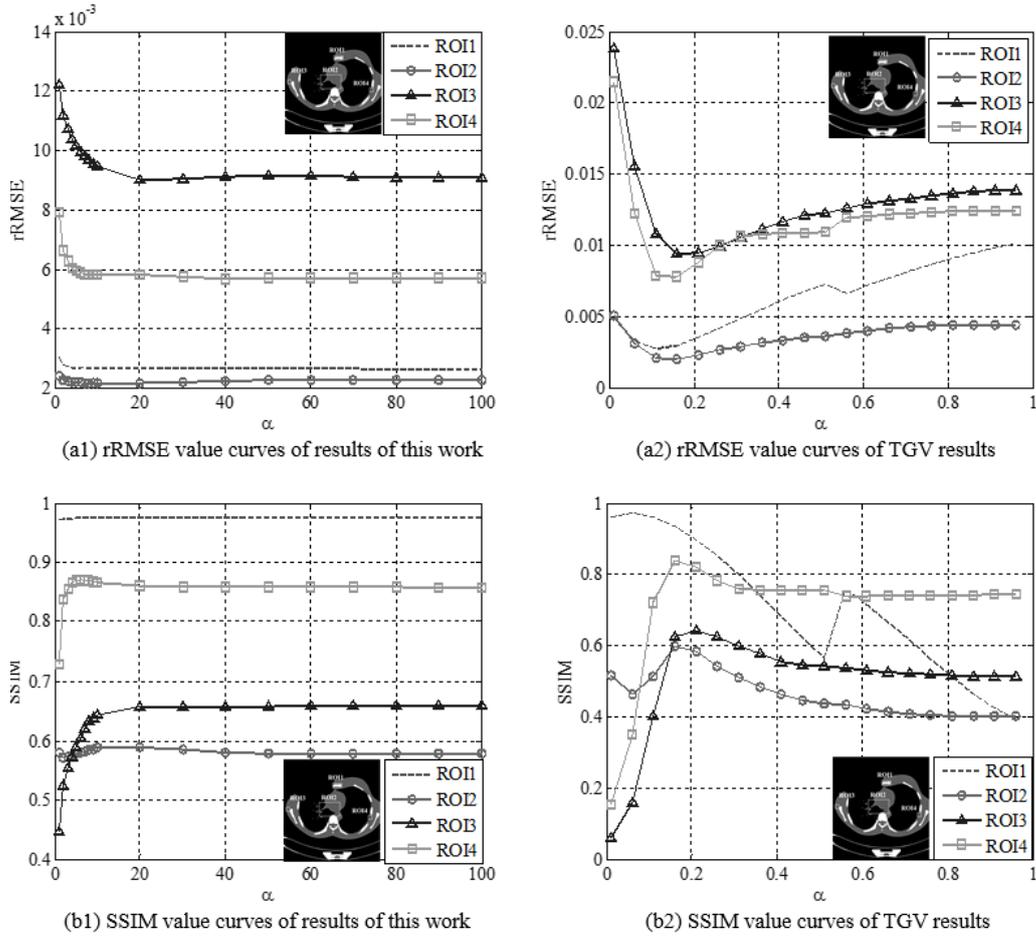
FIGURE 7. Four different ROI, the rRMSE and SSIM curves of results obtained by TGV and the proposed method as a function oflet α

than 0.9321, i.e., the SSIM value of the TV restoration image. In summary, from a quantitative point of view, the performance of the restoration image obtained by the proposed method is more satisfactory than that of the other three methods. Furthermore, this work analyzes the influence of parameter variation on the quality of the experimental results. The objective function of the algorithm in this work involves several parameters, and the main influencing factors are analyzed one by one. As the experimental results are of a similar quality, this work analyzes the influence of the common parameters of the proposed algorithm and the TGV method (iterations NUM2 and parameters α_1, α_0) on the quality of the experimental results. As shown in Fig.6, as the number of iterations NUM2 increases, the quality of the experimental results of the TGV algorithm and the proposed algorithm are found to improve and finally stabilize. When NUM2¿1500, the effect of the number of iterations NUM2 on the quality of the experimental results of the two algorithms diminishes and becomes almost negligible. Specifically, as shown in Fig. 6 (a), the rRMSE values of the two kinds of experimental results decrease with an increase in NUM2, and the rRMSE value of the experimental results obtained in this work is smaller. As shown in Fig. 6 (b), the PSNR values of the two kinds of experimental results increases with an increase in NUM2, and the PSNR value of the experimental result obtained by the proposed method is larger.

(a) Curve of λ when the number of particles T varies

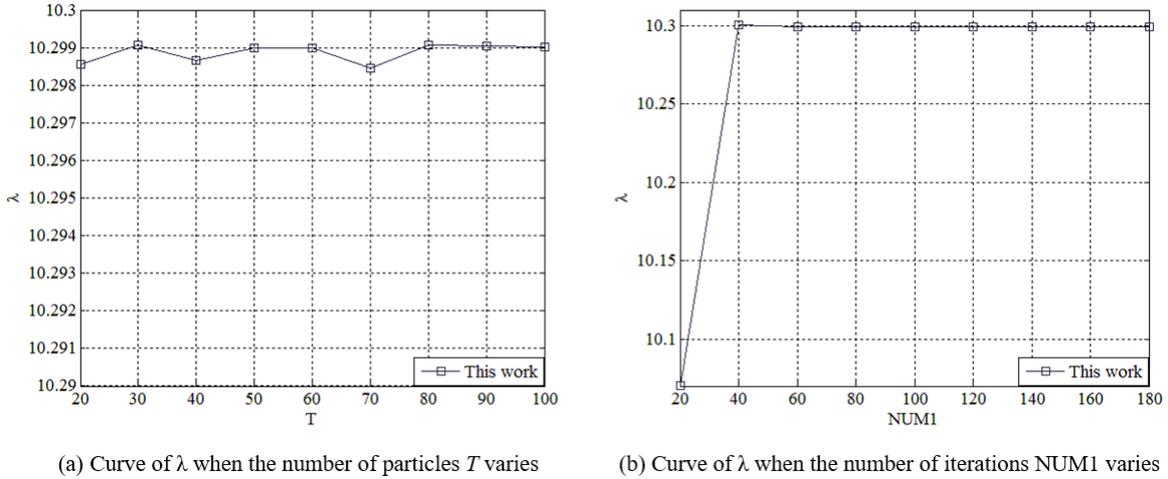(b) Curve of λ when the number of iterations NUM1 varies

FIGURE 8. Variation in the solution of the PSO algorithm as a function of the number of particles and the number of iterations.

As shown in Fig.7, let $\alpha_1 = \alpha_0 = \alpha$. With increasing α, the quality of the results obtained with the proposed algorithm improve and finally stabilize. When $\alpha > 20$, the effect of α on the quality of the results of this work results is reduced and becomes almost negligible. An increase in α leads to a gradual improvement in the quality of the TGV results to the best value before gradually worsening. When $\alpha = 0.18$, approximately, the quality of the TGV results reach a maximum. Specifically, for the four ROIs, as seen in Fig.7 (a1), the rRMSE curves display the same trend as α increases, where the rRMSE value of the experimental results obtained by the proposed method gradually becomes smaller and finally stabilizes. In the four ROIs, as seen in Fig.7 (b1), the trend of the SSIM curves is the same with increasing values of α, the SSIM value of the experimental results obtained by the proposed method gradually becomes larger and finally stabilizes. In the four ROIs, as seen in Fig.7 (a2), the rRMSE curves have the same trend with increasing values of α, where the rRMSE value of the experimental results obtained by the TGV method are first gradually reduced to reach an optimal value before gradually increasing. In the four ROIs, as seen in Fig.7 (b2), there are three ROIs with the same SSIM value curves, and all of them exhibit the same trend, i.e., first increasing and then decreasing. As the value of αincreases, the SSIM value of the experimental results obtained by the TGV method first gradually increases to an optimal value before gradually decreasing. The ROI with the different SSIM curve shows two increases and decreases, and the first time it increases to the maximum value. In summary, over the entire course of change, the performance of image quality and structural similarity in different ROIs of the results of TGV and the method proposed in this work are different. Within the same ROIs, the rRMSE values of the experimental results obtained by the proposed method are smaller and the SSIM values are larger.

The parameters of the proposed algorithm include the number of particles T and the number of iterations NUM1, both of which influence the quality of the graph of the experimental result mainly by influencing the value of the adaptive diffusion coefficient $c_S (\nabla u_N, \lambda)$. Next, we analyze the influence of the two parameters (T and NUM1) on the optimal solution of the PSO algorithm. As shown in Fig. 8 (a), if the number of particles T is larger than the number of independent variables, the increase in T has little effect on the optimal solution of the PSO algorithm. As shown in Fig.8 (b), we can see that
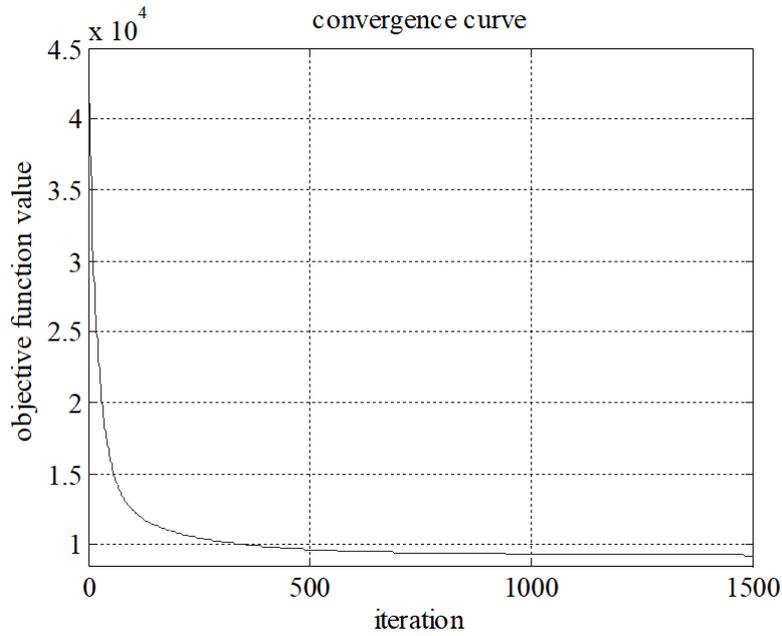
FIGURE 9. Value of the objective function of the proposed algorithm as a function of the number of iterative cycles NUM2.

an increase in the number of iterations NUM1 causes the PSO solution to increase and finally stabilize around 10.299. In addition, in this work the convergence of the algorithm is analyzed by plotting the change of the objective function value against the increase in the number of iterative cycles NUM2. As the iterative process advances (shown in Fig.9), the value of the objective function tends to stabilize and converge to a definite value. This shows that the proposed algorithm is feasible and converges to a stable solution.

4.2. **Pelvic CT experiments.** As shown in Fig. 10, different algorithms are used to filter the low-dose X-ray pelvic CT image, and the quality of the restoration images is different. Observing the first line of Fig.10, we can see that there are streak artifacts and noise residues in the restoration image obtained by the PM algorithm, but the image appears fuzzy during the smoothing process. Although the TV regularization method can suppress the noise and streak artifacts in the original low-dose pelvic image, it introduces new block artifacts, and the experimental results are unsatisfactory. Although the extent to which the noise and streak artifacts suppress the restoration image obtained by the TGV regularization method is considerable, the edge performance is unacceptable. In contrast, the proposed algorithm preserves the important edge features of the original low-dose image while suppressing noise and streak artifacts. The quality of the restoration image meets practical application requirements. Looking at the difference image shown in the second row of Fig.10, it can be seen that the noise and streak artifacts suppressed by the PM algorithm are limited during the smoothing process, and that some edges were smoothed during the process. The TV algorithm can suppress more noise and streak artifacts, and the edge preserving capability of TV is more effective than that of the PM algorithm. The extent to which noise and streak artifacts are filtered by the TGV algorithm exceeds that of the TV algorithm; however, the disadvantage is that some edges are also filtered. The proposed algorithm suppresses a large amount of noise and streak artifacts, and the extent to which important edges are smoothed is negligibly small. Looking at the difference image shown in the third row of Fig. 10, it can be found that
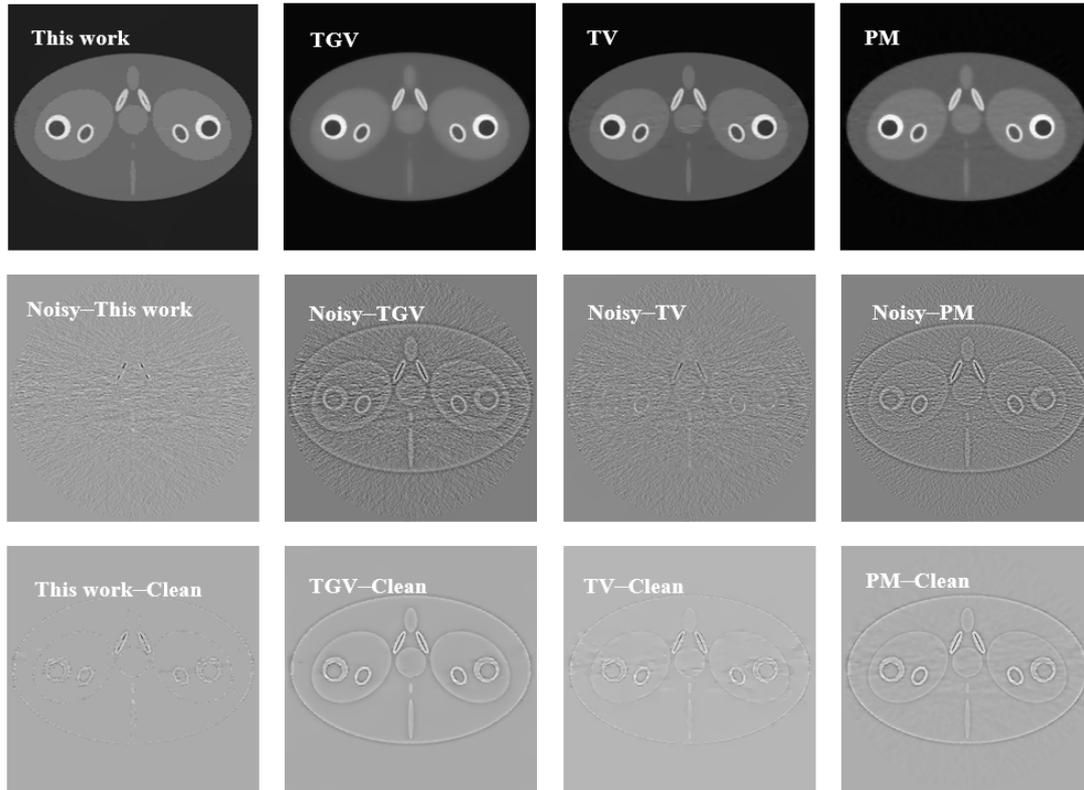
FIGURE 10. Pelvic results. First row: the four restoration images; second row: the difference images between the original low-dose image and the four restoration images; third row: the difference images between the four restoration images and the original standard dose image

TABLE 3. PSNR, rRMSE, and SSIM values of the three different ROIs of the four kinds of restoration images (shown in Fig.12)
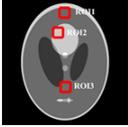
		ROI1			ROI2			ROI3	
	PSNR	rRMSE	SSIM	PSNR	rRMSE	SSIM	PSNR	rRMSE	SSIM
This work	25.9862	0.0020	0.9932	29.3480	0.0014	0.9943	24.4157	0.0013	0.8205
TGV	22.3501	0.0030	0.3805	23.4125	0.0027	0.5248	21.9800	0.0017	0.4998
TV	21.0846	0.0035	0.1971	19.7883	0.0041	0.2838	21.7985	0.0018	0.3370
PM	20.3441	0.0038	0.1065	19.6929	0.0042	0.1846	19.9957	0.0022	0.1795

the restoration image obtained by the PM algorithm contains streak artifacts and noise that are not present in the standard dose ideal image. The restoration image obtained by the TV algorithm contains block artifacts that are not present in the standard dose ideal image. Obviously, in the smoothing process, some edges of the original low-dose pelvic CT image are filtered out by the PM algorithm, TV algorithm, and TGV algorithm. The difference between the restoration image obtained by the proposed method and the ideal image is the least, and there are no obvious streak artifacts and noise residues. In summary, from a visual point of view, the quality of the restoration image obtained by the proposed algorithm is comparatively good.
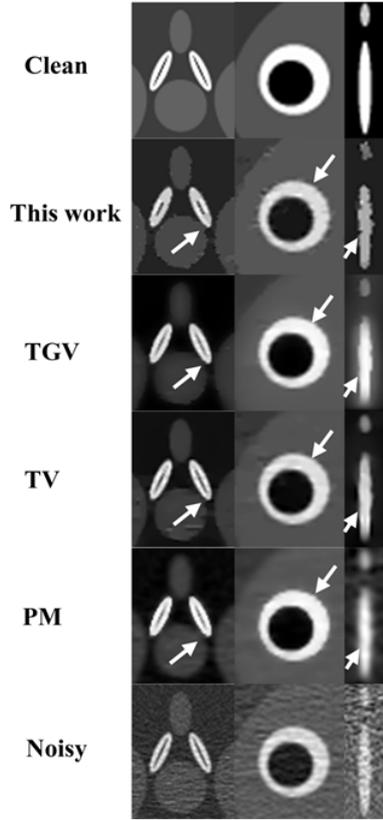
FIGURE 11. Partial enlargements of the pelvic restoration images obtained with the different methods (as shown in Fig. 10)

When observing the partially enlarged images (as shown in Fig.11) of the restoration images (shown in Fig.10), it can be seen that the main drawback of the PM algorithm is the appearance of fuzziness. The main disadvantage of the TV algorithm is that the processed image introduces block artifacts that are not present in the original low-dose image. Although the TGV algorithm can suppress the noise and streak artifacts effectively, the adaptive ability of the algorithm is limited. Compared with the other three algorithms, the superiority of the proposed algorithm is mainly reflected in the preservation of edges. Observing the area indicated by the white arrow in Fig.11, it can be found that the edges of the experimental results obtained by this work method behave well in different local regions of the pelvic model. In addition, Table.2 represents the PSNR, rRMSE, and SSIM values of the three different ROIs of the four kinds of restoration images (shown in Fig.10). In ROI1, the rRMSE value of the restoration image obtained by the proposed method is 0.0011, which is the same as that of the TGV restoration image; however, the PSNR value and the SSIM value of the restoration image obtained in our work are higher. It indicates that the restoration image obtained with our proposed method more closely resembles the standard dose image when the rRMSE values are the same. In ROI3, the rRMSE values of the restoration image obtained in this work and that of the TGV restoration image are also the same, with the corresponding SSIM of the restoration image obtained in this work being 0.9907, and the proposed method performs well in terms of structural similarity compared to the TGV restoration image. Compared with the experimental results obtained by the other three algorithms, the PSNR and SSIM values of the restoration image produced by the method proposed in this work are the

largest, and the rRMSE values are the smallest in each ROI. On the whole, in the three ROIs, compared with the other two indicators of the advantages of the restoration image obtained by the proposed method, the SSIM value is obviously superior.
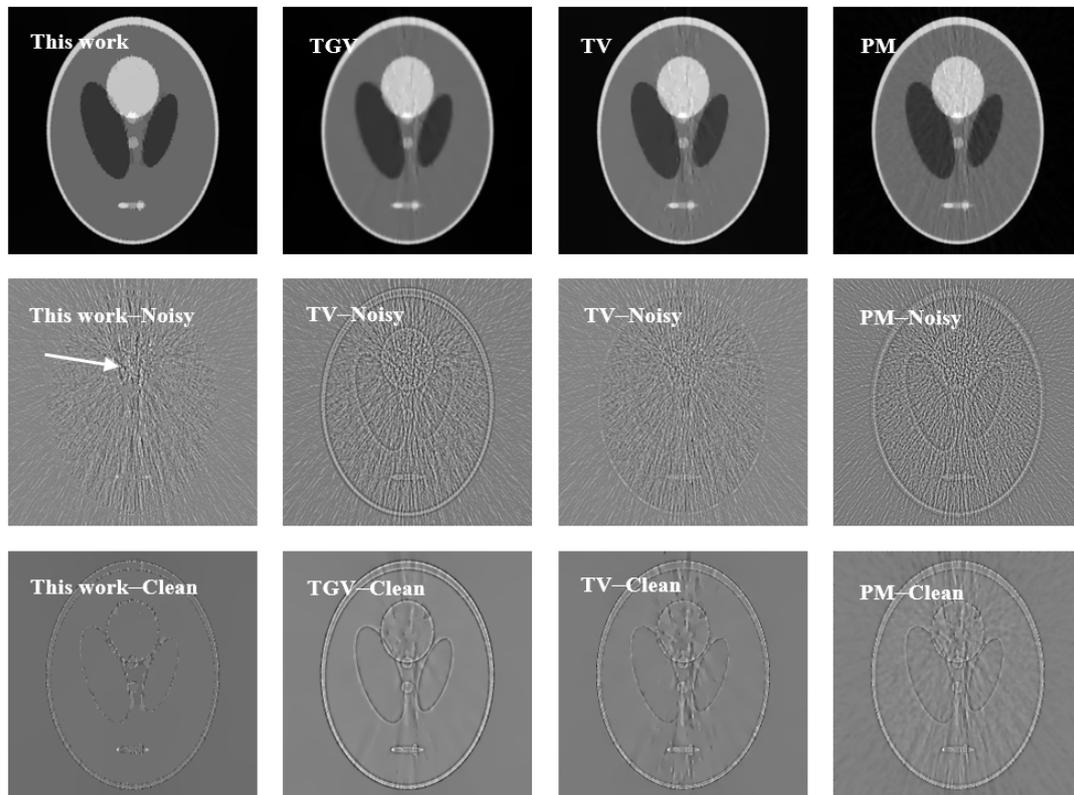

FIGURE 12. Modified Shepp-Logan head results. First row: four kinds of restoration images; second row: difference images between the original low-dose image and the four restoration images; third row: the difference images between the original four restoration images and the original standard dose image)

4.3. **Modified Shepp-Logan head CT experiments.** As shown in Fig. 12, different algorithms were used to filter the low-dose X-ray modified Shepp-Logan head image, and the quality of the restored image was different. In the first row in Figure 12, it can be found that some stripe artifacts remain near the mid-line of the reconstructed image in the PM algorithm. The TV regularization method suppresses most of the noise and stripe artifacts in the original low-dose modified Shepp-Logan head model, but causes the block artifacts at the same time. The TGV regularization method offers improved rejection of noise and stripe artifacts compared to the TV and PM algorithms, but its image edge-preserving ability is unsatisfactory. The proposed algorithm preserves the important edge features of original low-dose images while suppressing noise and streak artifacts and the quality of reconstructed images is good. In the second row in Fig.12, it can be seen that the artifacts of the low-dose modified Shepp-Logan head model image appear to be vertical stripes near the mid-line. In terms of the amount of removed artifacts and filtered noise, the algorithm described in this paper is superior. The strongly intense stripe artifacts near the vertical line are filtered out, as shown by the white arrows in the figure. As far as edge information retention is concerned, our proposed algorithm is also the best. The other three algorithms smoothed the edges of important structures of original low-level images

to a greater or lesser extent. The images in the third row of Fig.12 display many stripe artifacts and much noise neither of which are present in the ideal image near the vertical line in the restoration image of the PM algorithm, and there are block artifacts that are not present in the ideal image near the vertical line in the image restored by the TV algorithm. Obviously, in the smoothing process, the edge information of the original low-dose modified Shepp-Logan CT image is filtered out in the PM algorithm, TV algorithm, and TGV algorithm. For the proposed algorithm, the difference between the restored image and the ideal image is the least, and there are no obvious stripe artifacts and noise. In summary, from a visual point of view, the quality of the restored image obtained by this algorithm is superior. Observation of the localized enlargement of the restored image
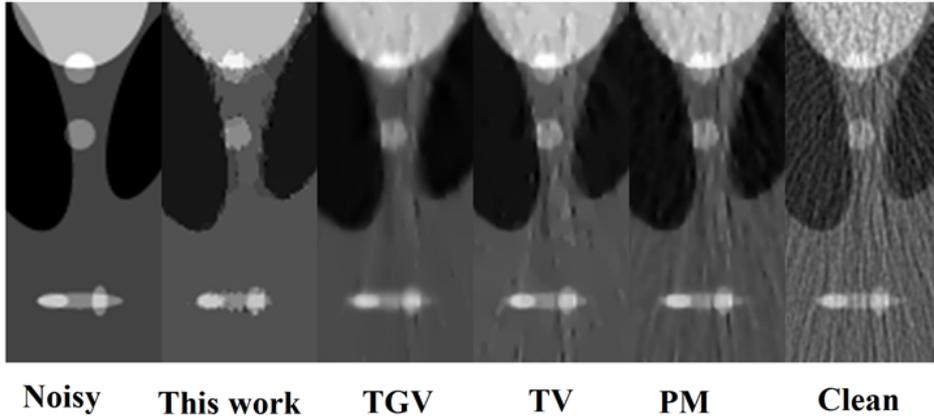

FIGURE 13. Partial enlargements of the modified Shepp-Logan head restoration images (as shown in Fig.12)

of the modified Shepp-Logan head model (shown in Fig.12), as shown in Fig.13, indicates that a large number of stripe artifacts and amount of noise remain in the image after processing by the PM algorithm. Clearly, the TV algorithm is more effective than the PM algorithm in suppressing noise and stripe artifacts, but its processed images contain block artifacts that are not present in the original low-dose image of the TV algorithm restoration image. The TGV algorithm smooths the important edges of the image while suppressing noise and streak artifacts. Compared with the other three algorithms, the ability of the proposed algorithm to suppress noise and streak artifacts is superior, and to a large extent it does not destroy the edges of important structures in the original low-dose images. Table.3 compares the performance of the four algorithms and contains the PSNR, rRMSE, and SSIM values for the four restoration images (shown in Fig.12) within three different ROIs. Because the streak artifacts in the original low-dose modified Shepp-Logan model are mainly distributed near the vertical line of the model, in terms of noise and artifact suppression ability, it is more likely that the ROI is selected near the mid-vertical line. In each ROI, compared with the other three algorithms, the proposed algorithm produces the largest and smallest values of the PSNR and SSIM, respectively. Obviously, within the three ROIs, the SSIM value of the restoration image of the proposed algorithm is far greater than that of the other three algorithms. This can also be explained in terms of the comparatively superior ability of this algorithm to remain at the edge of the structure.

5. **Conclusions.** In summary, the experimental results of different algorithms are closely related to the distribution characteristics of streak artifacts. The streak artifacts in different low-dose CT images have different shapes, different densities, and different distribution

densities. In particular, the low-dose thoracic CT images used in this work display horizontal and vertical streak artifacts with different orientations. The amplitude of artifacts in the middle region, in which the streak artifact distribution density is large, is close to the amplitude of the tissue structure. There is no obvious pattern of the distribution of streak artifacts. The artifacts of the low-dose pelvic model were mainly distributed in the horizontal direction, and the distribution intensity at the horizontal edge of the model was greater than that in the middle region. The artifacts of the low-dose modified Shepp-Logan head model are mainly distributed in the vertical direction, and are most dense in the vicinity of the vertical line in the model. The results of the algorithm proposed in this work show that the algorithm is feasible and effective, and has some advantages compared with other algorithms. Our experimental analysis revealed that the object to be processed by the low-dose CT image post-processing method is the low-dose image itself. Compared with the projection method and the reconstruction method, the post-processing method is computationally less complex and has lower operational cost. At the same time, because of the complexity, variability, and irregularity of the distribution of low-dose CT image artifacts, the post-processing methods are diversified and can be designed from many different angles to design low-dose CT images for different tissue site restoration methods.

<div align="center">

REFERENCES

</div>

[1] Cardiac CT imaging: diagnosis of cardiovascular disease, *Proceeding in Springer,* 2016.

[2] J. Hsieh, Computed tomography: principles, design, artifacts, and recent advances, *Proceeding in Bellingham,* WA: SPIE, 2009.

[3] Gartenschlger M, Schweden F, Gast K, et al. Pulmonary nodules: detection with low-dose vs conventional-dose spiral CT, *Journal of European radiology,* vol. 8, no. 4, pp. 609-614 , 1998.

[4] Pearce M S, Salotti J A, Little M P, et al. Radiation exposure from CT scans in childhood and subsequent risk of leukaemia and brain tumours: a retrospective cohort study, *Journal of The Lancet,* 2012, vol.380, no. 9840, pp. 499-505.

[5] Chen Y, Shi L, Feng Q, et al. Artifact suppressed dictionary learning for low-dose CT image processing, *Journal of IEEE transactions on medical imaging,* 2014, vol. 33, no. 12, pp. 2271-2292.

[6] Chen Y, Yang Z, Hu Y, et al. Thoracic low-dose CT image processing using an artifact suppressed large-scale nonlocal means, *Journal of Physics in Medicine and Biology,* 2012, vol. 57, no. 9, pp. 2667.

[7] Beister M, Kolditz D, Kalender W A. Iterative reconstruction methods in X-ray CT, *Journal of Physica medica,* 2012, vol. 28, no. 2, pp. 94-108.

[8] Xiao C, Stoel B C, Bakker M E, et al. Pulmonary Fissure Detection in CT Images Using a Derivative of Stick Filter, *Journal of IEEE transactions on medical imaging,* 2016, vol. 35, no. 6, pp. 1488-1500.

[9] Niu S, Gao Y, Bian Z, et al. Sparse-view x-ray CT reconstruction via total generalized variation regularization, *Journal of Physics in medicine and biology,* 2014, vol. 59, no. 12, pp. 2997.

[10] Guo W, Qin J, Yin W. A new detail-preserving regularization scheme, *Journal of SIAM Journal on Imaging Sciences,* 2014, vol. 7, no. 2, pp. 1309-1334.

[11] Li Z, Yu L, Trzasko J D, et al. Adaptive nonlocal means filtering based on local noise level for CT denoising, *Journal of Medical physics,* 2014, vol. 41, no. 1, pp. 011908.

[12] Elad M, Aharon M. Image denoising via sparse and redundant representations over learned dictionaries, *Journal of IEEE Transactions on Image processing,* 2006, vol. 15, no. 12, pp. 3736-3745.

[13] Chen H, Zhang Y, Zhang W, et al. Low-dose CT denoising with convolutional neural network, *Journal of arXiv preprint arXiv:1610.00321,* 2016.

[14] Cui X Y, Gui Z G, Zhang Q, et al. Learning-Based Artifact Removal via Image Decomposition for Low-dose Computed Tomography Image Processing, *Journal of IEEE Transactions on Nuclear Science*, 2016:1-1.

[15] Ha S, Mueller K. Low dose CT image restoration using a database of image patches., *Journal of Physics in Medicine and Biology*, 2015, vol. 60, no. 2, pp. 869-82.

[16] Zhang A, Jiang H, Ma L, et al. A Shearlet-based algorithm for quantum noise removal in low-dose CT images, *SPIE Medical Imaging. International Society for Optics and Photonics*, 2016: 97843O-97843O-7.

[17] Shi L, Hu Y, Chen Y, et al. Improving Low-dose Cardiac CT Images based on 3D Sparse Representation, *Journal of Scientific reports,* 2016, 6.

[18] Chen Y, Yin X, Shi L, et al. Improving abdomen tumor low-dose CT images using a fast dictionary learning based processing, *Journal of Physics in medicine and biology*, 2013, vol. 58, no. 16, pp. 5803.

[19] Valkonen T, Bredies K, Knoll F. Total generalized variation in diffusion tensor imaging, *Journal of SIAM Journal on Imaging Sciences*, 2013, vol. 6, no. 1, pp. 487-525.

[20] Bredies K, Kunisch K, Pock T. Total generalized variation, *Journal of SIAM Journal on Imaging Sciences*, 2010, vol. 3, no. 3, pp. 492-526.

[21] Knoll F, Bredies K, Pock T, et al. Second order total generalized variation , no. TGV) for MRI, *Journal of Magnetic resonance in medicine*, 2011, vol. 65, no. 2, pp. 480-491.

[22] Duan J, Lu W, Pan Z, et al. New second order MumfordShah model based on -convergence approximation for image processing, *Journal of Infrared Physics and Technology*, 2016, vol. 76, pp. 641-647.

[23] Lu C, Wang M. Alternating direction method for TGV-TGV* based cartoon-texture image decomposition, *Journal of IET Image Processing*, 2016, vol. 10, no. 6, pp. 495-504.

[24] Aubert G, Kornprobst P. Mathematical problems in image processing: partial differential equations and the calculus of variations *[M]. Springer Science and Business Media*, 2006.

[25] Rudin L I, Osher S, Fatemi E. Nonlinear total variation based noise removal algorithms, *Journal of Physica D: Nonlinear Phenomena*, 1992, vol. 60, no. 1, pp. 259-268.

[26] Bredies K, Valkonen T. Inverse problems with second-order total generalized variation constraints, *Journal of Proceedings of SampTA*, 2011, 2011.

[27] Vlachos I K, Sergiadis G D. The role of entropy in intuitionistic fuzzy contrast enhancement, *International Fuzzy Systems Association World Congress. Springer Berlin Heidelberg*, 2007, pp. 104-113.

[28] Nguyen H. A novel similarity/dissimilarity measure for intuitionistic fuzzy sets and its application in pattern recognition, *Journal of Expert Systems with Applications*, 2016, vol. 45, pp. 97-107.

[29] Nguyen H. A new knowledge-based measure for intuitionistic fuzzy sets and its application in multiple attribute group decision making, *Journal of Expert Systems with Applications*, 2015, vol. 42, no. 22, pp. 8766-8774.

[30] Song Y, Wang X, Lei L, et al. A novel similarity measure on intuitionistic fuzzy sets with its applications, *Journal of Applied Intelligence*, 2015, vol. 42, no. 2, pp. 252-261.

[31] Jing L, Min S. Some entropy measures of interval-valued intuitionistic fuzzy sets and their applications, *Journal of Adv. Model. Optim*, 2013, vol. 15, no. 2, pp. 211-221.

[32] Wei C P, Gao Z H, Guo T T. An intuitionistic fuzzy entropy measure based on trigonometric function, *Journal of Control and Decision*, 2012, vol. 27, no. 4, pp. 571-574.

[33] Li J, Deng G, Li H, et al. The relationship between similarity measure and entropy of intuitionistic fuzzy sets, *Journal of Information Sciences*, 2012, vol. 188, pp. 314-321.

[34] Wan S, Dong J. A possibility degree method for interval-valued intuitionistic fuzzy multi-attribute group decision making, *Journal of Journal of Computer and System Sciences*, 2014, vol. 80, no. 1, pp. 237-256.

[35] Xiao Z, Chen W, Li L. A method based on interval-valued fuzzy soft set for multi-attribute group decision-making problems under uncertain environment, *Journal of Knowledge and information systems*, 2013, vol. 34, no. 3, pp. 653-669.

[36] Fan X, Lei Y, Wang Y, et al. Long-term intuitionistic fuzzy time series forecasting model based on vector quantisation and curve similarity measure, *Journal of IET Signal Processing*, 2016.

[37] Fan X, Lei Y, Li C, et al. Strict intuitionistic fuzzy entropy, *Journal of Systems Engineering and Electronics*, 2016, vol. 38, no. 3, pp. 602-606.

[38] Burger W, Burge M J. Digital image processing: an algorithmic introduction using Java[M]. Springer, 2016.

[39] Gui Z, Liu Y, He J. PML algorithm for positron emission tomography combined with nonlocal fuzzy anisotropic diffusion filtering, *Journal of IEEE Transactions on nuclear science*, 2012, vol. 59, no. 5, pp. 1984-1989.

[40] Xia S, Huang Y, Peng S, et al. Adaptive anisotropic diffusion for noise reduction of phase images in Fourier domain Doppler optical coherence tomography, *Journal of Biomedical Optics Express*, 2016, vol. 7, no. 8, pp. 2912-2926.

[41] Chen R C, Yu P T. Fuzzy selection filters for image restoration with neural learning, *Journal of IEEE transactions on signal processing*, 1999, vol. 47, no. 5, pp. 1446-1450.

[42] Pal S K, Ghosh A. Fuzzy geometry in image analysis, *Journal of Fuzzy Sets and Systems*, 1992, vol. 48, no. 1, pp. 23-40.

[43] Vlachos I K, Sergiadis G D. Inner product based entropy in the intuitionistic fuzzy setting, *Journal of International Journal of Uncertainty, Fuzziness and Knowledge-Based Systems*, 2006, vol. 14, no. 03, pp. 351-366.

[44] Kennedy J. Particle swarm optimization[M]//Encyclopedia of machine learning. Springer US, 2011, pp. 760-766.

[45] Esmin A A A, Coelho R A, Matwin S. A review on particle swarm optimization algorithm and its variants to clustering high-dimensional data, *Journal of Artificial Intelligence Review*, 2015, vol. 44, no. 1, pp. 23-45.

[46] Perona P, Malik J. Scale-space and edge detection using anisotropic diffusion, *Journal of Pattern Analysis and Machine Intelligence, IEEE Transactions on*, 1990, vol. 12, no. 7, pp. 629-639.